Solvothermal Synthesis and Photoluminescent Properties of ZnS/Cyclohexylamine: Inorganic−Organic Hybrid Semiconductor Nanowires

Libo Fan, Hongwei Song,* Haifeng Zhao, Guohui Pan, Hongquan Yu, Xue Bai, Suwen Li, Yanqiang Lei, Qilin Dai, Ruifei Qin, Tie Wang, Biao Dong, Zhuhong Zheng, and Xinguang Ren

Key Laboratory of Excited-State Physics, Changchun Institute of Optics, Fine Mechanics, and Physics, Chinese Academy of Sciences, 16 Eastern South-Lake Road, Changchun 130033 and Graduate School of Chinese Academy of Sciences, Beijing 100039, P. R. China

Received: January 23, 2006; In Final Form: March 25, 2006

An inorganic−organic hybrid semiconductor, ZnS/CHA (CHA = cyclohexylamine) nanocomposites was successfully synthesized via a solvothermal method using CHA as solvent, which yielded uniform and ultralong nanowires with widths of 100−1000 nm and lengths of 5−20 μm. Changing the reaction conditions could alter the morphology and optical properties of the nanocomposites. The periodic layer subnanometer structures were identified by high-resolution transmission electron microscopy (HR-TEM) images, with thickness of ∼2 nm. The composites exhibited a very large blue-shift in their optical absorption edge as well as an exciton excitation band due to a strong quantum confinement effect caused by the internal subnanometer-scale structures. The pure hexagonal wurtzite ZnS nanowires were also obtained by extracting the ZnS/CHA nanocomposites with dimethyl formamide (DMF). In addition, the luminescent properties of exciton and defect-related transitions in different samples of ZnS/CHA were discussed in detail.

I. Introduction

Quantum confinement effect has shown its huge charm in optoelectronic applications and ultrasensitive biological detection. Currently, semiconductor dots are referred because a very large variation is achievable in these applications.[1−5] However, it is a great challenge to generate uniform and periodic lattices of dots. It is well-known that inorganic frameworks have rigidity and stability, while organic and coordination compounds hold great promises for processability, flexibility, structural diversity, and geometrical controllability. Incorporation of the two counterparts into a single structure may generate organic−inorganic hybrid composites that enhance or combine the useful properties of both components.[6−10] Some experiments have been done to explore this kind of inorganic−organic hybrid nanomaterials, including clay, metal chalcogenides, metal halides, metal oxides, and metal phosphates and phosphonates.[11−15] Recently, developments demonstrate that unique hybrid II−VI semiconductors can be also synthesized by incorporating segments of a II−VI semiconductor and organic species in one structure via coordinate or covalent bonds such as $ZnS(en)_{0.5}$, $MnSe(pda)_{0.5}$, $ZnTe(N_2H_4)$, and $CdSe(en)_{0.5}$, etc.[16−22]

Actually, the organic template may dominate the structure of the inorganic−organic hybrid semiconductors. By choosing an organic template, various low-dimensional nanostructures can be obtained, such as nanobelts, nanosheets, nanorods, etc, which would be crucial for certain devices in nanodevices.[11,17,19,21,23] On the other hand, in the inorganic−organic hybrid semiconductors due to incorporating of inorganic and organic materials, there generally exists subnanometer structure in the period of several nanometers, leading to obvious confinement effects.[11,24]

Recently, we prepared uniform and ultralong ZnS/CHA hybrid nanowires via a solvothermal method using cyclohexylamine (CHA) as solvent for the first time. The composites exhibited a remarkable blue-shift in their optical absorption edge as well as an exciton excitation band due to a strong quantum confinement effect induced by the internal layer substructures. In this paper, we systematically reported the preparation, characterization, and spectral properties of the wire-like ZnS/CHA nanocomposite. The pure hexagonal wurtzite ZnS nanowires were also obtained using the ZnS/CHA nanocomposite precursor.

II. Experiments

A. Sample Preparation. Zinc acetate and thiourea were analytical-grade reagents and CHA was a chemical-grade reagent, which were all used as received without further purification. In a typical synthesis, 17 mL of 0.03 M $Zn(CH_3COO)_2 \cdot 2H_2O$ and 18 mL of 0.06 M $(NH_2)_2CS$ aqueous solution was added into 420 mL CHA at room temperature under magnetic stirring. A transparent solution formed after stirring for 30 min. The resultant solution was transferred into 14 50-mL Teflon-lined stainless steel autoclaves on average and then maintained at 120 °C for 20 h in an oven. After the reaction, the Teflon-lined autoclaves were cooled naturally to room temperature. The product was collected and washed with ethanol several times to remove the reactants possibly remaining in the final products. Then half of the white precipitate was centrifugated and dried at 80−90 °C for 12 h in vacuum, which was called sample **A**. Another half product was redispersed in 60 mL of DMF under magnetic stirring for 30 min to extract it. The final suspension was transferred into two 50-mL Teflon-lined stainless steel autoclaves on average and maintained at 180 °C for 48 h in an oven. Then the product was cooled,

* Corresponding author. E-mail: hwsong2005@yahoo.com.cn. Fax: 86-431-6176320.

10.1021/jp0604589 CCC: $33.50
Published on Web 06/15/2006

TABLE 1: Reaction Conditions of Different Samples and Their Fluorescent Decay Time Constants as Well as the Proportion of the Component with Shorter Decay Constant of the Exciton and Defect Emissions

			A	B	C	D	E
reaction conditions	reactant quantity (mmol)	$Zn(CH_3COO)_2 \cdot 2H_2O$	0.255	0.255	0.255	4.25	0.255
		$(NH_2)_2CS$	0.54	0.54	0.54	9.0	0.54
	solvent	$V_{water}:V_{CHA}$	1:12	1:12	0:13	1:12	1:12
	temperature (°C)		120	100	120	120	120
	extraction using DMF		no	no	no	no	yes
life time	exciton emission	τ_1 (ns)	2.9	0.31	0.23		1.1
		τ_2 (ns)	6.0	4.1	3.8	5.3	6.9
		R_1 (%)	71	27	20	0	54
	defect emission	τ_1 (ns)	1.7	1.6	1.7		1.2
		τ_2 (ns)	11.0	9.3	10.6	8.3	6.7
		R_1 (%)	40	26	26	0	54

washed, centrifugated, and dried just like **A**, which was called sample **E**. Similarly, 8.5 mL of 0.03 M $Zn(CH_3COO)_2 \cdot 2H_2O$ and 9.0 mL of 0.06 M $(NH_2)_2CS$ aqueous solution was added into 210 mL of CHA and reacted at 100 °C for 20 h, forming sample **B**. Sample **C** was produced by adding 0.056 g of $Zn(CH_3COO)_2 \cdot 2H_2O$ (0.255 mmol) and 0.041 g of $(NH_2)_2CS$ (0.54 mmol) into 227.5 mL of CHA without deionized water at 120 °C for 20 h. Sample **D** was obtained by adding 8.5 mL of 0.5 M $Zn(CH_3COO)_2 \cdot 2H_2O$ and 9.0 mL of 1.0 M $(NH_2)_2CS$ aqueous solution into 210 mL of CHA at 120 °C for 20 h. The processes of stir, cooling, washing, centrifugation, and drying of samples **B**, **C**, and **D** were the same as **A**. In comparison, the reaction conditions of all samples were listed in Table 1.

B. Measurements. The data of X-ray diffraction (XRD) patterns were obtained on a Rigaku D/Max 2500V PC diffractometer operated at 18 kW with Cu Kα radiation ($\lambda = 1.5406$ Å). Field-emission scanning electron microscopy (FE-SEM) images were measured on XL30 ESEM FEG (FEI Company). HR-TEM images were recorded on a JEM-3010 transmission electron microscope. The Fourier transformation−infrared spectra (FT−IR) were recorded on a Bio-Rad FTS-3000 (Excalibur Series). A Perkin-Elmer Pyris Diamond thermogravimetric analyzer (with a heating rate of 10 °C/min, 40−800 °C) was used for the thermal degradation study of samples under nitrogen atmosphere, i.e., thermogravimetric analysis (TGA).

The powder samples were redispersed in the ethanol by ultrasound to form a suspension for the measurement of the UV−vis absorption spectra, which were measured on an UV-3101PC UV−Vis−NIR scanning spectrophotometer (Shimadzu). Fluorescence and excitation spectra were recorded on a Hitachi F-4500 spectrophotometer equipped with a 150-W Xe-arc lamp at room temperature. Fluorescent dynamics were measured on an FL920-Fluorescence Lifetime spectrometer (Edinburgh Instruments) with MCP-PMT, in which the excitation source was an NF900 nanosecond flash lamp with a pulse duration of 1 ns. By the deconvolution taking into account of the lamp pulse width and the instrumental temporary response, the resolution limitation of the system reached to ∼100 ps.

III. Characterization

A. XRD Patterns. The XRD patterns of various samples were depicted in Figure 1. As one can see from Figure 1, the samples of **A**, **B**, **C**, and **D** have almost the same XRD patterns, implying that they have similar crystal structure. However, the relative intensities of the sharp diffraction peaks vary significantly in different samples, which indicates that the crystallinity in different samples is different. The sharper and stronger diffraction peaks correspond to better crystallinity. In comparison to the sample **E**, we know that most of the sharp peaks have obvious correlation with the well-crystallized precursors. The XRD patterns of the sample **E** indicate that it is phase-pure ZnS with hexagonal wurtzite structure (JCPDS 36-1450). The especially narrower and stronger peak at the (002) face implies that the preferential growth is along the *c*-axis. Estimated from the peak half widths at (110), (103), and (112) planes by using the Scherrer equation, the average crystalline size of ZnS is ∼3 nm. In comparison to the XRD patterns of **E**, the diffraction patterns at (002) plane of ZnS might be identified in the ZnS/CHA composites, which were labeled with arrows. In addition, the patterns at (110), (103), and (112) planes seemed to appear in some samples; however, they were too weak to detect clearly.

B. FE-SEM and TEM Images. Figure 2 depicts the FE-SEM images of different samples. Figure 2a demonstrates that sample **A** yields ultralong nanowires, with diameters of ∼100 nm and lengths of 15−20 μm. Figure 2f demonstrates that, in sample **A**, the wires are uniform and with smooth surfaces and regular cross section (circle). Figure 2b shows that by reducing the temperature from 120 °C (**A**) to 100 °C (**B**), the diameters of the nanowires hardly change; however, the lengths become shorter (5−10 μm). Actually, temperature is has key role in the formation of nanowires. It is found that 90−130 °C is a suitable range for the growth of nanowires. As the temperature becomes lower than 90 °C, the reaction hardly takes place. As the temperature becomes higher than 130 °C, nanoclusters form. In Figure 2c, it can be observed that the products are still wire-like in sample **C**; however, they become shorter, irregular, and less uniform. This indicates that a suitable quantity of water is important to form perfect nanowires. Our investigation also indicates that, when the volume ratio of water to CHA (V_{water}:

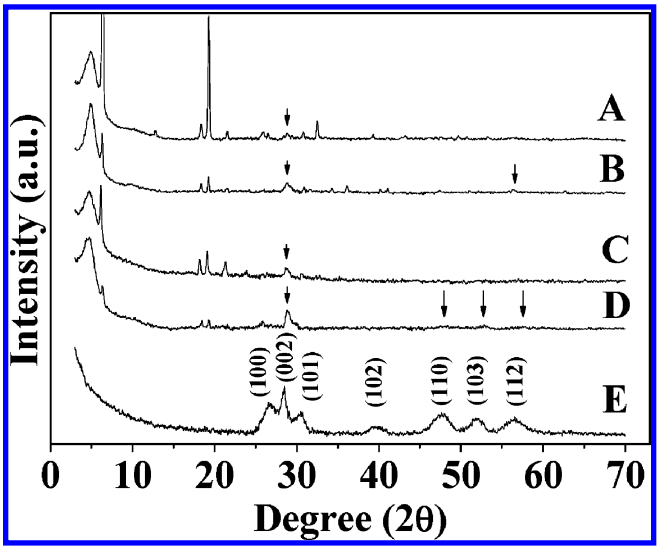

Figure 1. XRD patterns of different ZnS/CHA or ZnS nanowires.

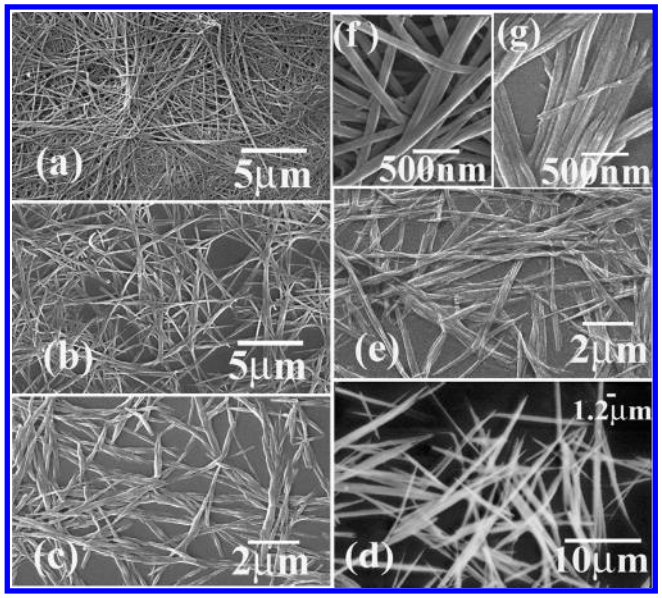

Figure 2. FE-SEM images of (a) sample **A**, (b) sample **B**, (c) sample **C** (d) sample **D**, and (e) sample **E**; (f) high-magnification images of sample **A** and (g) high-magnification images of sample **E**.

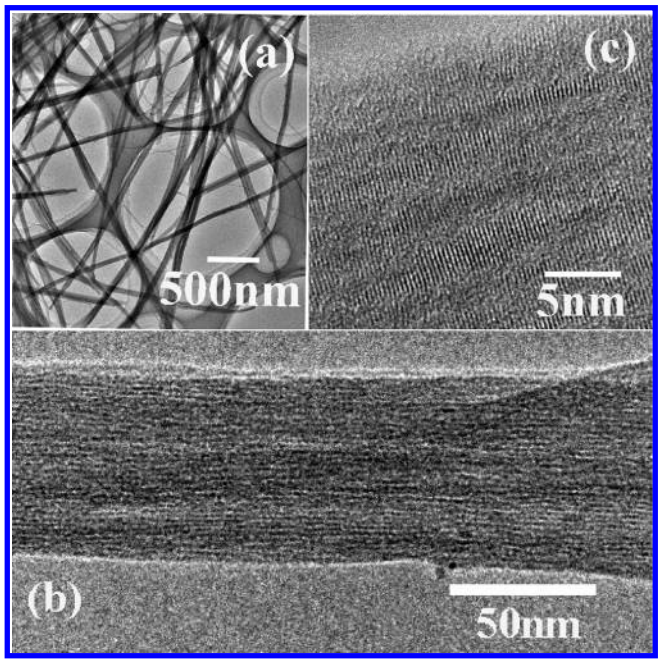

Figure 3. (a) TEM and (b, c) HR-TEM images of sample **A**.

V_{CHA}) is higher than 1:8, the nanoclusters form. When the concentration of the reactants in **A** increases by 16 times, the obtained nanowires (**D**) become fatter. As can be seen in Figure 2d, the diameter of **D** increases to ~1 μm and the length remains at ~15 μm. Note that, by decreasing the concentration of the reactants in the aqueous solution further, the tender nanowires form. From Figure 2e and g, it can be seen that the ZnS powders obtained from ZnS/CHA precursor still yield nanowires; however, the surface and the cross section of the nanowires become irregular.

Figure 3a depicts TEM images of the sample **A** and parts b and c of Figure 3 depict HR-TEM images of an individual nanowire. Figure 3a shows that the morphology of **A** is uniform and wire-like just like its FE-SEM images. Figure 3b clearly demonstrates that the periodic layer arrays formed in the individual nanowire. Calculation shows that the period is ~2 nm. Figure 3c further indicates that the layer structure formed by interlaced arrangement of the amorphous and crystalline bands, which looks like the ordered assembly of ZnS nanorods reported previously.[25] According to the figure, the interplanar distance in the crystalline area is estimated to be 3.125 Å, which exactly corresponds to the (002) plane of the wurtzite ZnS (lattice constants of the bulk wurtzite ZnS are $a = 3.820$ Å and $c = 6.257$ Å). According to HR-TEM images, it is suggested that the interlaced arrangement of wurtzite ZnS and amorphous CHA forms layer structures in the ZnS/CHA composites.

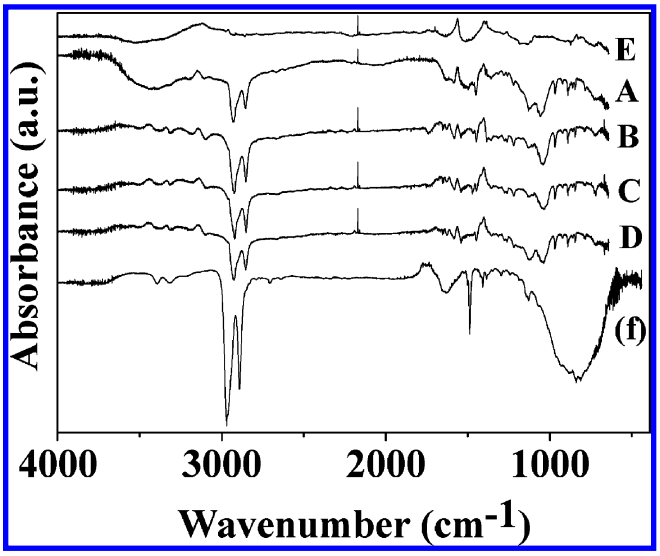

Figure 4. FT-IR absorption spectra of different samples.

C. FT-IR Spectra. Figure 4 shows FT-IR spectra of the ZnS/CHA composites in comparison to pure CHA solution. The spectrum of pure CHA (Figure 4f) gives the typical absorbance of the C−H vibrations at 2969 and 2893 cm^{-1}.[25,26] These vibrations also appear in the ZnS/CHA composites but shift to 2924 and 2854 cm^{-1}. The appearance of the C−H vibrations evidences the presence of the organic component. The shift is caused by the chemical bonding behavior between ZnS and CHA.[24,25] The likeness of IR spectra of different ZnS/CHA composites indicate that they have the similar component and the same bonding strength between ZnS and CHA. In sample **E**, C−H vibrations are not observed, which illustrates further that pure ZnS nanowires are extracted from ZnS/CHA precursors.

D. TGA Results. To determine the thermal stabilization of the ZnS/CHA and the content of CHA in different samples, the TGA experiment was performed. As displayed in Figure 5, we can see that the hybrid composite is stable at temperatures below 200 °C and CHA is gradually lost over 200 °C. The weight loss is completed at ~660 °C. The content of CHA is nearly the same in **A** and **C**, but is smaller in **D**. Assuming the chemical formula of the ZnS/CHA composite as $ZnS\cdot(CHA)_x$, x is deduced to be 1.36 for sample **A**, 1.24 for **C**, and 0.75 for **D**. From the above XRD and FT−IR, following UV−Vis absorption and PL results and the same reactant concentration of **A**, **B**, and **C**, we can conclude that the content of CHA in **B** is similar to that in **A** and **C**.

E. Possible Formation Mechanism of Nanowires. A fundamental understanding of the formation mechanism of ZnS/CHA hybrid nanowires is crucial to control the whole chemical reaction. In fact, we can simply consider a quasi-emulsion system formed after adding water into CHA in which the amount of water plays a key role. When a certain quantity of water

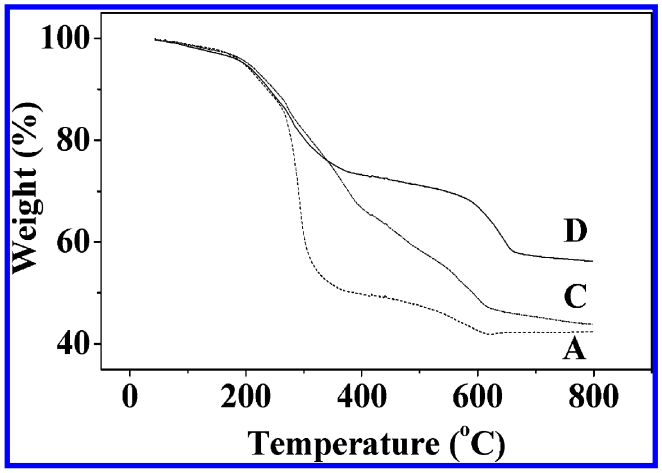

Figure 5. TGA curves of samples **A**, **C**, and **D**.

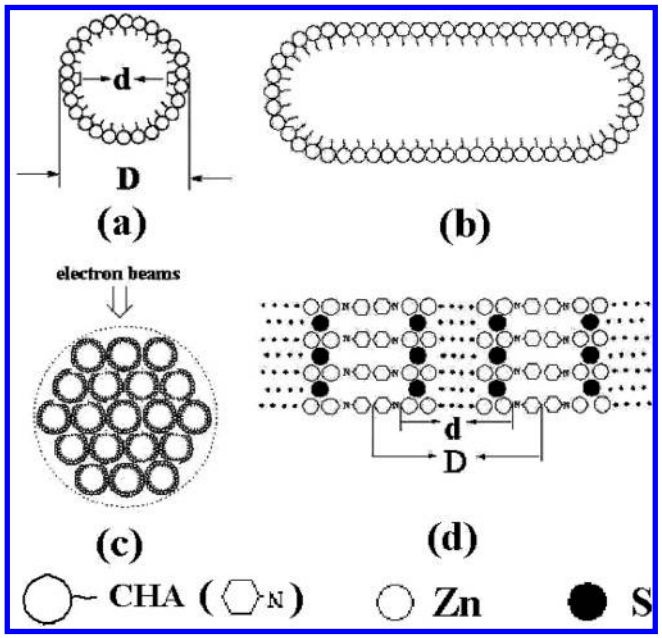

Figure 6. Schematic illustration of a possible mechanism for the formation of ZnS/CHA nanowires. The cross section of (a) short axis and (b) the long axis of single reverse micelle; (c) the cross section of short axis and (d) the microstructure of one ZnS/CHA nanowire.

was added into CHA, a great number of reverse micelles containing water solution formed and served as microreaction containers. Coordinate bonds formed between $-NH_2$ of CHA and Zn^{2+} inside the reverse micelles. Different reverse micelles self-organized together by the attraction of polarized CHA along the long and short axis of micelles, forming wire-like structure. The polarization of CHA was caused by the existence of $-NH_2$ bonds in the carbon rings. Under certain solvothermal conditions, S^{2-} was released from thiourea. In this case, ZnS formed subsequently and grew along the reverse micelles. The schematic illustration of a possible mechanism for the formation of ZnS/CHA nanowires is drawn in Figure 6. In the TEM experiments, because the electron beams were induced perpendicularly to the length direction of a nanowire, layer structures were observed.

In the preparation, adding of proper water was significant for the formation of ZnS/CHA nanowires. As proper water was added, uniform and regular nanowires were obtained (samples **A**, **B**, and **D**), while in the preparation without water, irregular nanowires formed (sample **C**). In the later case, a quasi-emulsion system could also form. However, the reverse micelles contained the reactants only instead of the mixture of water and reactants. Those reverse micells were not so stable as in the former case. In the hydrothermal conditions, the reaction resulted in the loss of the reactants, and the nanowires obtained were therefore shorter, irregular, and less uniform. As excess water was added, it existed in continuous phase and the reverse micells did not form, thus the morphology of the products was irregular.

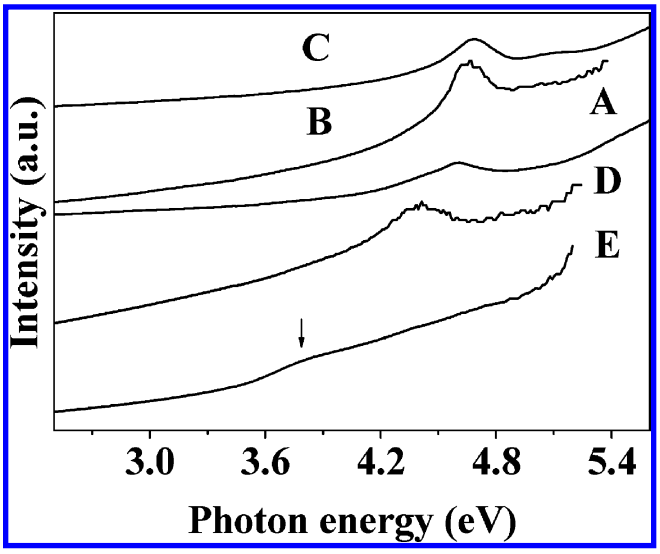

Figure 7. UV−Vis absorption spectra of various samples.

Suited hydrothermal temperature range (90−130 °C) was also a key factor for the formation of nanowires. If the temperature was lower than this range, the reaction cannot take place. If the temperature was higher, reverse micells could be destroyed by the quick thermomovement of all molecules, and irregular products formed. In the temperature range, the nanowires become longer with increasing temperature.

IV. Optical Properties

A. UV−Vis Absorption Spectra. The UV−vis absorption spectra of various samples are depicted in Figure 7. As shown, the pure ZnS nanowires (**E**) have a slight absorption peak at 3.79 eV, which is consistent with the band gap of bulk wurtzite ZnS.[27,28] Quantum confinement effect occurs in the case of the nanoparticles when the particle size becomes comparable with or smaller than the exciton Bohr radius.[29,30] The exciton Bohr radius in ZnS is 2.5 nm.[21,31,32] It is natural that the quantum confinement effect does not occur in **E** because the diameter of the ZnS nanowires (∼100 nm) is much larger than the exciton Bohr radius in ZnS. In the ZnS/CHA composites, the band gap absorption blue-shifts in comparison to the bulk and becomes stronger in comparison to the bulk. The energies of the band gap absorption in the samples **A**, **B**, **C**, and **D** were 4.60, 4.67, 4.68, and 4.40 eV, respectively. The blue-shift of the band gap absorption in ZnS/CHA composites can be attributed to the quantum confinement effect. In the ZnS/CHA composites, despite the diameter of the nanowires being ∼100 nm, however, in the nanowires there exist periodic subnanometer structures forming by an interlaced arrangement of ZnS and CHA layers along the *c*-axis of ZnS, which is clearly identified by the HR-TEM figures. Moreover, the thickness of the periodic ZnS layers is about several nanometers, which is smaller than the exciton Bohr radius in ZnS (in sample **A**, the average thickness of the ZnS layers is deduced to be ∼2 nm). As a consequence, strong confinement effects occur in the ZnS/CHA composites.

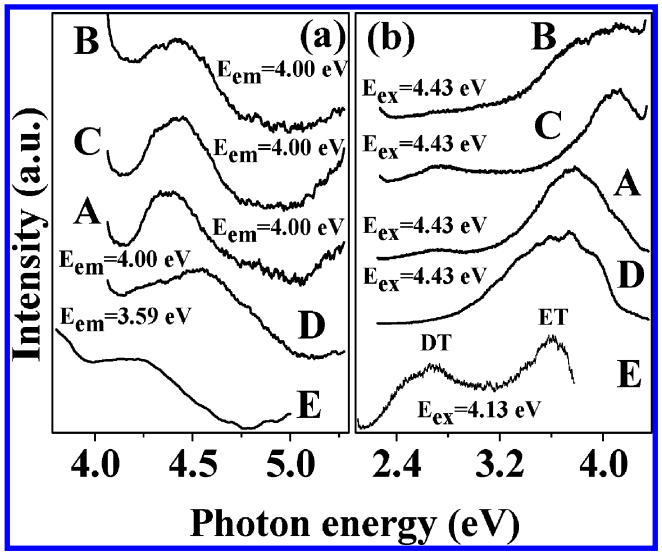

Figure 8. (a) Excitation and (b) emission spectra of various samples. In the figure, ET and DT represent exciton transition and defect transition, respectively.

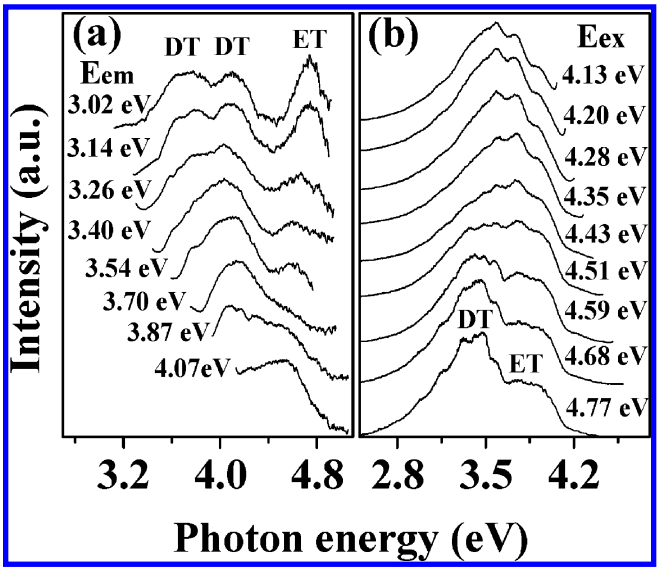

Figure 9. (a) Excitation spectra of sample **D** as monitoring at different energies and (b) emission spectra of sample **D** under different excitation energies. (ET represents exciton transition and DT means defect transition).

The contrast studies on different ZnS/CHA composites suggest that the confinement effect is nearly independent of the diameter of the nanowires as it varies in the range of 100−1000 nm, but strongly dependent on the ratio of CHA to ZnS in the ZnS/CHA composites. Greater content of CHA in ZnS/CHA composites induces a larger blue-shift in absorption spectra. We suggest that the content of CHA can modify the thickness of the ZnS layers. Increased content of CHA leads the average thickness of the ZnS layers to decrease, inducing a stronger confinement effect.

B. Luminescence. Parts a and b of Figure 8 show the PL excitation and emission spectra in different samples, respectively. In Figure 8a, the peak energies are 4.38 eV (**A**), 4.42 eV (**B**), 4.45 eV (**C**), 4.56 eV (**D**), and 4.21 eV (**E**), respectively, which shift red compared to the absorption spectra. In comparison to the pure ZnS (sample **E**), the excitation peaks for the ZnS/CHA composites shift blue due to the confinement effect, just like the results of absorption spectra. In Figure 8b, there appear two peaks for all the samples, assigned to the exciton emission (high-energy side) and the defect emission. The defect emission at 2.70 eV in **A**, **B**, **C**, and **E** is caused by trapped surface states.[25,33−36] In the sample **D**, we did not observe the above defect emission, but observed the defect emission at 3.44 eV caused by sulfur vacancy and interstitial sulfur lattice defects, which will be discussed later.[25,34,37,38] In comparison to the pure ZnS nanowires, the exciton emission in the ZnS/CHA composite demonstrated blue-shift. For the samples **A**, **B**, **C**, **D**, and **E**, the peak energies locate at 3.77, 4.10, 4.13, 3.69, and 3.61 eV, respectively. On the contrary, the energy (∼2.70 eV) of the defect emission has little variation. The ratio of the defect emission to the exciton emission varies considerably in different samples. In pure ZnS, the ratio of the defect emission to the exciton emission increases more greatly than those in the ZnS/CHA composites, indicating that more defects are involved after extracting.

In comparison to the other samples, the photoluminescence for sample **D** demonstrates special emission properties. As a special case, energy-selective excitation experiments were performed on sample **D**. Figure 9a shows excitation spectra at different monitoring energies, while Figure 9b displays the emission spectra under different excitation energies. In Figure 9b, as the excitation energy is in the range of 4.59−4.77 eV, two emission bands are distinguished, which are assigned to the exciton transition (high-energy side) and the defect transition caused by sulfur vacancy and interstitial sulfur lattice defects, respectively. As the excitation energy is in the range of 4.13−4.51 eV, the boundary between the exciton band and defect band disappears and they unite as one band. This phenomenon may come from the energy transfer between the two transitions. In Figure 9a, three excitation peaks at 3.69, 4.08, and 4.74 eV are identified as monitoring 3.02 and 3.14 eV. The emission at 3.02 and 3.14 eV should be dominantly contributed to defect transition, as shown in Figure 9b. In the excitation spectra, the 3.69 and 4.08 eV peaks should be assigned to the defect transitions, while the 4.74 eV peak is assigned to the exciton transition. As monitoring defect emissions, the exciton excitation peak appears, indicating that energy transfer from exciton to defect states occurs.

C. Fluorescence Dynamics. Fluorescence dynamics of the exciton and the defect emissions in different samples were also measured, as shown in Figure 10a and b. It can be seen that all emissions have a lifetime on the nanosecond time scale as report previously.[39−41] The fluorescence decay curves in different samples vary greatly. In most of the samples, the fluorescence decays biexponentially, while in sample **D**, it decays exponentially. The two exponential time constants, τ_1 (shorter) and τ_2 and the relative contribution of the component with a shorter lifetime, are listed in Table 1. The longer lifetimes for the exciton emission are in the range of 3.8−6.9 ns, while those for the defect emission are in the range of 6.7−11.0 ns. The shorter lifetimes are in the range of 0.23−2.9 ns for the exciton transition and 1.2−1.7 ns for the defect emissions. For samples **B** and **C**, the lifetimes are shorter than those in the other samples, especially for the shorter lifetime of the exciton emission. There are a number of factors influencing the florescence decays. The lifetime constant is dominated by the sum of radiative and nonradiative transition rates. On one hand, the distribution, energy, and number of defect states influence significantly the energy transfer between exciton and defect states or difference

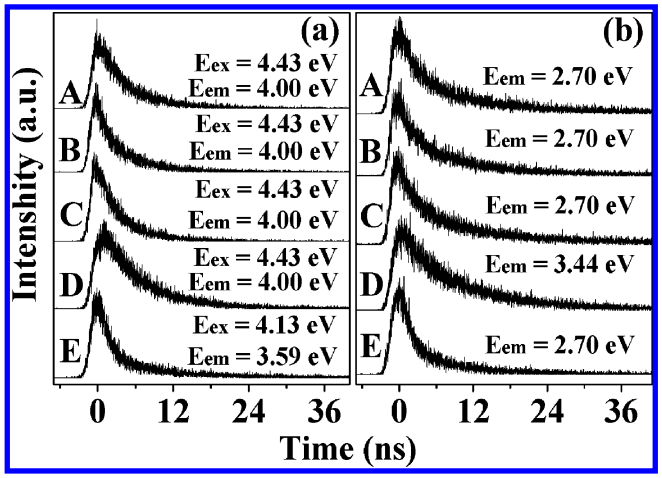

Figure 10. Fluorescent decay curves of (a) exciton emission and (b) defect emission in different samples.

defect states, leading to the variation of the nonradiative transition rate. On the other hand, the radiative transition rate in ZnS/CHA may change due to the confinement effect. The strong confinement effect might induce a increased radiative transition rate, leading the fluorescent lifetime to decrease.[5,42] Presently, we cannot determine what contributions are for the radaitive and nonradiative transitions in different samples, which should be studied further.

V. Conclusions

ZnS/CHA inorganic−organic hybrid semiconductor composites as well as phase-pure hexagonal wurtzite ZnS were prepared by the solvothermal method and characterized by XRD patterns, FE-SEM and HR-TEM images, FT−IR spectra, and TGA. The results demonstrate that they have uniform and wirelike morphology with lengths of 5−20 μm. By changing the different reaction conditions, we can tailor their diameters from 100 nm to 1 μm. Periodic subnanometer-layer structures were clearly identified by HR-TEM figures, forming by interlaced arrangement of wurtzite ZnS and amorphous CHA. The thickness of the layer ZnS was estimated to be ∼2 nm, which was smaller than the exciton Bohr radius in ZnS (2.5 nm). Because of the existence of the quantum confinement effect caused by subnanometer structure, the band gap absorption and exciton excitation energy in ZnS/CHA nanocomposites demonstrated ra emarkable blue-shift in comparison to the bulk. Systematic studies indicate that the confinement effect is nearly independent of the size of the nanowires in the studied range, but strongly dependent on the ratio of ZnS to CHA. The increase of CHA in the ZnS/CHA leads to the improvement of the confinement effect. Above all, the uniform morphology and unique optical properties of these ZnS/CHA hybrid nanowires could offer a wider application in optoelectronic or biological areas in the future.

Acknowledgment. We gratefully thank the financial support of the National Natural Science Foundation of China (grant nos. 10374086 and 10504030) and Talent Youth Foundation of Jilin Province (grant no. 20040105).

References and Notes

(1) Henglein, A. *Chem. Rev.* **1989**, *89*, 1861.
(2) Nirmal, M.; Brus, L. E. *Science* **1996**, *271*, 933.
(3) Bruchez, M., Jr.; Moronne, M.; Gin, P.; Weiss, S.; Alivisatos, A. P. *Science* **1998**, *281*, 2013.
(4) Chan, W. C. W.; Nie, S. M. *Science* **1998**, *281*, 2016.
(5) Chen, L.; Zhang, J.; Luo, S.; Lu, S.; Wang, X. *Appl. Phys. Lett.* **2004**, *84*, 112.
(6) Mann, S.; Ozin, G. *Nature* **1996**, *382*, 313.
(7) Batten, S. R.; Robson, R. *Angew. Chem., Int. Ed.* **1998**, *37*, 1460.
(8) Kagan, C. R.; Mitzi, D. B.; Dimitrakopoulos, C. D. *Science* **1999**, *286*, 945.
(9) O'Keeffe, M.; Eddaoudi, M.; Li, H.; Reineke, T.; Yaghi, O. M. *J. Solid State Chem.* **2000**, *152*, 3.
(10) Huang, X. Y.; Li, J.; Fu, H. X. *J. Am. Chem. Soc.* **2000**, *122*, 8789.
(11) Yao, W. T.; Yu, S. H.; Huang, X. Y.; Jiang, J.; Zhao, L. Q.; Pan, L.; Li, J. *Adv. Mater.* **2005**, *17*, 2799.
(12) Alberti, G.; Costantino, U. In *Comprehensive Supramolecular Chemistry*; Atwood, J. L., Davies, J. E. D., MacNicol, D. D., Vögtle, F., Eds.; Elsevier Science: New York, 1996; Vol. 7, Chapter 1, pp 1−24.
(13) Seitz, M.; Kaiser, A.; Stempfhuber, S.; Zabel, M.; Reiser, O. *J. Am. Chem.* Soc. **2004**, *126*, 11426.
(14) Rajic, N.; Logar, N. Z.; Mali, G.; Kaucic, V. *Chem. Mater.* **2003**, *15*, 3734.
(15) Schubert, U.; Volkel, T.; Moszner, N. *Chem. Mater.* **2001**, *13*, 3811.
(16) Huang, X. Y.; Heulings, H. R., IV; Le, V.; Li, J. *Chem. Mater.* **2001**, *13*, 3754.
(17) Yu, S. H.; Yoshimura, M. *Adv. Mater.* **2002**, *14*, 296.
(18) Huang, X. Y.; Li, J.; Zhang, Y.; Mascarenhas, A. *J. Am. Chem. Soc.* **2003**, *125*, 7049.
(19) Dong, Y. J.; Peng, Q.; Li, Y. D. *Inorg. Chem. Commun.* **2004**, *7*, 370.
(20) Li, J. P.; Xu, Y.; Wu, D.; Sun, Y. H. *Solid State Commun.* **2004**, *130*, 619.
(21) Yao, W. T.; Yu, S. H.; Pan, L.; Li, J.; Wu, Q. S.; Zhang, L.; Jiang, J. *Small* **2005** *1*, 320.
(22) Heulings, H. R., IV; Huang, X.; Li, J.; Yuen, T.; Lin, C. L. *Nano Lett.* **2001**, *1*, 521.
(23) Chen, X. J.; Xu, H. F.; Xu, N. S.; Zhao, F. H.; Lin, W. J.; Lin, G.; Fu, Y. L.; Huang, Z. L.; Wang, H. Z.; Wu, M. M. *Inorg. Chem.* **2003**, *42*, 3100.
(24) Deng, Z. X.; Wang, C.; Sun, X. M.; Li, Y. D. *Inorg. Chem.* **2002**, *41*, 869.
(25) Li, Y. C.; Li, X. H.; Yang, C. H.; Li, Y. F. *J. Phys. Chem. B* **2004**, *108*, 16002.
(26) Rana, R. K.; Zhang, L. Z.; Yu, J. C.; Mastai, Y.; Gedanken, A. *Langmuir* **2003**, *19*, 5904.
(27) Pankove, J. I. *Optical Processes in Semiconductors*; Dover Publications Inc.: New York, 1970.
(28) Trindade, T.; O'Brien, P.; Pickett, N. L.*Chem. Mater.* **2001**, *13*, 3843.
(29) Vogel, W.; Borse, P. H.; Deshmukh, N.; Kulkarni, S. K. *Langmuir* **2000**, *16*, 2032.
(30) Du, H.; Chen, C.; Krishnan, R.; Krauss, T. D.; Harbold, J. M.; Wise, F. W.; Thomas, M. G.; Silcox, J. *Nano Lett.* **2002**, *2*, 1321.
(31) Rossetti, R.; Hull, R.; Gibson, J. M.; Brus, L. E. *J. Chem. Phys.* **1985**, *82*, 552.
(32) Arul Dhas, N.; Zaban, A.; Gedanken, A. *Chem. Mater.* **1999**, *11*, 806.
(33) Meng, X. M.; Liu, J.; Jiang, Y.; Chen, W. W.; Lee, C. S.; Bello, I.; Lee, S. T. *Chem. Phys. Lett.* **2003**, *382*, 434.
(34) Wageh, S.; Ling, Z. S.; Rong, X. X. *J. Cryst. Growth* **2003**, *255*, 332.
(35) Li, Y. Q.; Zapien, J. A.; Shan, Y. Y.; Liu, Y. K.; Lee, S. T. *Appl. Phys. Lett.* **2006**, *88*, 013115.
(36) Chae, W. S.; Yoon, J. H.; Yu, H.; Jang, D. J.; Kim, Y. R. *J. Phys. Chem. B* **2004**, *108*, 11509.
(37) Zhao, Y.; Hong, J. M.; Zhu, J. J. *J. Cryst. Growth* **2004**, *270*, 438.
(38) Jiang, X. C.; Xie, Y.; Lu, J.; Zhu, L. Y.; He, W.; Qian, Y. T. *Chem. Mater.* **2001**, *13*, 1213.
(39) Becker, W. G.; Bard, A. J. *J. Phys. Chem. B* **1983**, *87*, 4888.
(40) Sooklal, K.; Cullum, B. S.; Angel, S. M.; Murphy, C. J. *J. Phys. Chem.* **1996**, *100*, 4551.
(41) Chung, J. H.; Ah, C. S.; Jang, D. J. *J. Phys. Chem. B* **2001**, *105*, 4128.
(42) Bhargava, R. N.; Gallagher, D.; Hong, X.; Nurmikko, A. *Phys. Rev. Lett.* **1994**, *72*, 416.